arXiv:1605.07971v5 [cond-mat.str-el] 14 Sep 2016

Chirality-induced magnon transport in AA-stacked bilayer honeycomb magnets

S. A. Owerre[1,2]

[1] *Perimeter Institute for Theoretical Physics, 31 Caroline St. N., Waterloo, Ontario N2L 2Y5, Canada.**
[2] *African Institute for Mathematical Sciences, 6 Melrose Road, Muizenberg, Cape Town 7945, South Africa.*

In this Letter, we study the magnetic transport in AA-stacked bilayer honeycomb chiral magnets coupled either ferromagnetically or antiferromagnetically. For both couplings, we observe chirality-induced gaps, chiral protected edge states, magnon Hall and magnon spin Nernst effects of magnetic spin excitations. For ferromagnetically coupled layers, thermal Hall and spin Nernst conductivities do not change sign as function of magnetic field or temperature similar to single-layer honeycomb ferromagnetic insulator. In contrast, for antiferromagnetically coupled layers, we observe a sign change in the thermal Hall and spin Nernst conductivities as the magnetic field is reversed. We discuss possible experimental accessible honeycomb bilayer quantum materials in which these effects can be observed.

Online supplementary data available from stacks.iop.org/JPhysCM/28/47LT02/mmedia

I. INTRODUCTION

The subject of chirality is ubiquitous in many branches of physics. It plays a prominent role in the understanding of many physical systems, in particular magnetic systems. Recently, the influence of spin chirality in magnon excitations of ordered quantum magnetic materials has attracted considerable attention. Chirality-induced topological magnetic systems exhibit novel properties [1–10] similar to topological insulators in electronic systems [11–13]. In these systems, the propagation of collective excitations (magnons) is similar to spin-orbit coupling induced propagation in non-interacting electronic systems. However, non-interacting magnons can propagate without dissipation as they are uncharged quasiparticles. This property is crucial for future dissipationless magnon transport [2, 14–16]. In magnetic structures with corner sharing triangles, chirality is induced by the Dzyaloshinsky-Moriya interaction (DMI) [17] and spin scalar chirality is defined as $\chi_{ijk} = \mathbf{S}_i \cdot (\mathbf{S}_j \times \mathbf{S}_k)$, where (i, j, k) label sites on the triangular plaquettes of the lattice and $\mathbf{S}_i$ is the spin at site i.

Recently, chirality-induced transports have been observed in two-dimensional (2D) single-layer kagome magnet Cu(1-3, bdc) [18, 19]. Also in a number of 3D single-layer chiral ferromagnetic pyrochlores such as $Lu_2V_2O_7$, $Ho_2V_2O_7$, and $In_2Mn_2O_7$ [2, 4]. For ferromagnetic pyrochlores, thermal Hall conductivity changes sign upon reversing the direction of magnetic field, whereas for kagome magnet thermal Hall conductivity changes sign as function of magnetic field or temperature. There has been a great interest in these chirality-induced topologically protected magnetic systems [20–23]. Recently, chirality-induced magnetic bilayer-skyrmion lattice has been shown to exhibit novel properties completely different from single-layer skyrmions [8]. However, transport properties of chirality-induced magnetic bilayer magnons have not been addressed in many chiral magnetic systems.

In this Letter, we study the chirality-induced magnetic transport in AA-stacked bilayer honeycomb chiral magnet coupled either ferromagnetically or antiferromagnetically. For ferromagnetically coupled layers, we compute the thermal Hall conductivity κ_{xy}, which shows a similar trend to that of single-layer honeycomb ferromagnetic insulator [21, 22] with no sign change. In contrast, for antiferromagnetically coupled layers, we observe a sign change in the thermal Hall conductivity and spin Nernst conductivity [24] as the magnetic field is reversed. We show that fully antiferromagnetically coupled bilayer with ordered Néel state exhibits similar properties to that of antiferromagnetically coupled bilayer ferromagnets. These results suggest an experimental search for chirality-induced bilayer honeycomb chiral magnets. In fact, many experimental realizations of bilayer honeycomb-lattice systems have been reported. They include magnetic compounds such as $CrBr_3$ [25, 26] which is a spin-1/2 bilayer honeycomb ferromagnetic materials. $Na_3Cu_2SbO_6$ [27] and β-$Cu_2V_2O_7$ [28] are spin-1/2 Heisenberg antiferromagnetic materials, in each of which the $S = 1/2$ Cu^{2+} ions are situated on the sites of weakly coupled honeycomb-lattice layers. Besides, the iridates A_2IrO_3 (A= Na, Li) [29, 30] have magnetically ordered Mott phases in which the Ir^{4+} ions form effective $S = 1/2$ moments arrayed on weakly-coupled honeycomb-lattice layers. In these honeycomb-lattice materials, spin chirality or DMI can be induced using many experimental growth techniques and our results can be confirmed directly.

II. BILAYER FERROMAGNETIC INSULATOR

The Hamiltonian for AA-stacked bilayer honeycomb chiral magnet shown in Fig. 1(a) is given by

$$H = H^{\tau}_{FM} + H^{\tau}_{DM} + H^{\tau}_{ext.} + H_{inter} \tag{1}$$

*Electronic address: sowerre@perimeterinstitute.ca

where

$$H^{\tau}_{FM} = -J\sum_{\langle i,j\rangle}\mathbf{S}^{\tau}_i\cdot\mathbf{S}^{\tau}_j - J'\sum_{\langle\langle i,j\rangle\rangle}\mathbf{S}^{\tau}_i\cdot\mathbf{S}^{\tau}_j \quad (2)$$

$$H^{\tau}_{DM} = \sum_{\langle\langle i,j\rangle\rangle}\mathbf{D}_{ij}\cdot\mathbf{S}^{\tau}_i\times\mathbf{S}^{\tau}_j;\ H^{\tau}_{ext.} = -h\sum_i S^{\tau}_{i,z}, \quad (3)$$

$$H_{inter.} = -J_{\perp}\sum_i \mathbf{S}^{T}_i\cdot\mathbf{S}^{B}_i, \quad (4)$$

where τ denotes the top (T) and bottom (B) layers. $\mathbf{S}_i$ is the spin moment at site i, $J>0$ is a nearest-neighbour (NN) ferromagnetic interaction on each layer, $J'>0$ is a next-nearest-neighbour (NNN) ferromagnetic interaction on each layer, and $\mathbf{D}_{ij}$ is the DMI vector between site i and j, allowed by the NNN triangular plaquettes on the honeycomb lattice, where $\mathbf{D}_{ij}=\nu_{ij}\mathbf{D}$, and $\nu_{ij}=\pm1$. The Zeeman magnetic field is h in units of $g\mu_B$. The interaction $J_{\perp}>0$ represents the ferromagnetic or antiferromagnetic ($J_{\perp}<0$) interlayer coupling.

III. MAGNON BANDS

A. Ferromagnetic interlayer coupling

For ferromagnetic interlayer coupling $J_{\perp}>0$, the Fourier space Hamiltonian of the Holstein-Primakoff [31] boson operators is given by $H=\sum_{\mathbf{k}}\psi^{\dagger}_{\mathbf{k}}\cdot\mathcal{H}(\mathbf{k})\cdot\psi_{\mathbf{k}}$ where $\psi^{\dagger}_{\mathbf{k}}=(a^{\dagger}_{\mathbf{k}A_1}, a^{\dagger}_{\mathbf{k}B_1}, a^{\dagger}_{\mathbf{k}A_2}, a^{\dagger}_{\mathbf{k}B_2})$, and

$$\mathcal{H}_{FM}(\mathbf{k}) = \epsilon_a\tau_0\otimes\sigma_0 + \tau_0\otimes\sigma_z m_{\mathbf{k}\phi} - v_s\tau_0\otimes(f_{\mathbf{k}}\sigma_+ + f^{*}_{\mathbf{k}}\sigma_-) - v_{\perp}\tau_x\otimes\sigma_0, \quad (5)$$

where $\boldsymbol{\sigma}$ and $\boldsymbol{\tau}$ are triplet pseudo-spin Pauli matrices for the sublattice and layer degrees of freedom respectively, τ_0 and σ_0 are identity matrices in each space, and $\sigma_{\pm}=(\sigma_x\pm i\sigma_y)/2$; $v_0=h+zv_s+z'v'_s$, $v_s(v'_s)(v_D)(v_{\perp})=JS(J'S)(DS)(J_{\perp}S)$, $v_t=\sqrt{v'^2_s+v^2_D}$, $z(z')=3(6)$, and $\epsilon_a=v_0+v_{\perp}-2v_t\sum_{\mu}\cos(\mathbf{k}\cdot\mathbf{a}_{\mu})\cos\phi$. Here, $f_{\mathbf{k}}=e^{ik_y a/2}\left(2\cos\sqrt{3}k_x a/2+e^{-3ik_y a/2}\right)$, and $m_{\mathbf{k}\phi}=2v_t\sum_{\mu}\sin(\mathbf{k}\cdot\mathbf{a}_{\mu})\sin\phi$, where $\mathbf{a}_1=\sqrt{3}\hat{x}$; $\mathbf{a}_2=(-\sqrt{3}\hat{x},3\hat{y})/2$ $\mathbf{a}_3=-(\sqrt{3}\hat{x},3\hat{y})/2$. We have assumed a DMI along the z-axis. The phase factor $\phi=\arctan(D/J')$ is a magnetic flux generated by the DMI on the NNN triangular plaquettes. The eigenvalues are given by

$$\epsilon_{\alpha\pm}(\mathbf{k}) = \epsilon_a + (-1)^{\alpha}v_{\perp} \pm \sqrt{m^2_{\mathbf{k}\phi}+|v_s f_{\mathbf{k}}|^2}, \quad (6)$$

where $\alpha=1,2$ is the layer index. For $v_{\perp}=0$, the Hamiltonian decouples to two single layers [21]. The magnon band is shown in Fig. 2(a). At the Dirac points $\mathbf{K}_{\pm}=(\pm4\pi/3\sqrt{3}a,0)$, the eigenvalues reduces to $\epsilon_{\alpha\pm}(\mathbf{K}_{\pm})=\epsilon_a+(-1)^{\alpha}v_{\perp}\pm|m_{\phi}|$, where $m_{\phi}=3\sqrt{3}v_t\sin\phi$. This is similar to AA-stacked spin-orbit-coupled bilayer graphene [32, 33].

B. Antiferromagnetic interlayer coupling

We now consider antiferromagnetically coupled layers, with the spins on the upper or lower layer pointing downwards, and the interlayer coupling $J_{\perp}<0$. The top and bottom layers are still ferromagnetic insulators described by H^{τ}_{FM} and H^{τ}_{DM}. To study the magnetic excitations, we perform a π-rotation about the S_x-axis on the top layer,

$$S^x_i \to S^x_i,\ S^y_i\to -S^y_i,\ S^z_i\to -S^z_i. \quad (7)$$

This rotation keeps the upper ferromagnetic layer invariant but points the spins in the new z-direction, and changes the sign of H^{τ}_{ext} and H^{τ}_{DM} on the top layer. The Fourier space Hamiltonian is $H=\frac{1}{2}\sum_{\mathbf{k}}\Psi^{\dagger}_{\mathbf{k}}\mathcal{H}_{AFM}(\mathbf{k})\Psi_{\mathbf{k}}+\text{const.}$, where $\Psi_{\mathbf{k}}=(\psi^{\dagger}_{\mathbf{k}},\ \psi_{-\mathbf{k}})$, and

$$\mathcal{H}_{AFM}(\mathbf{k}) = \begin{pmatrix}\mathcal{A}(\mathbf{k}) & \mathcal{B}\\ \mathcal{B} & \mathcal{A}^{*}(-\mathbf{k})\end{pmatrix}. \quad (8)$$

The matrices $\mathcal{A}(\mathbf{k})$ and $\mathcal{B}$ are given by

$$\mathcal{A}(\mathbf{k}) = \epsilon_0\tau_0\otimes\sigma_0 + \tau_z\otimes\sigma_z m_{\mathbf{k}\phi} - v_s\tau_0\otimes(f_{\mathbf{k}}\sigma_+ + f^{*}_{\mathbf{k}}\sigma_-) + h\tau_z\otimes\sigma_0;\ \mathcal{B}=|v_{\perp}|\tau_x\otimes\sigma_0, \quad (9)$$

where $\epsilon_0 = zv_s + z'v'_s + |v_{\perp}| - 2v_t\sum_{\mu}\cos(\mathbf{k}\cdot\mathbf{a}_{\mu})\cos\phi$. Note that $\mathcal{A}(\mathbf{k})\neq\mathcal{A}^{*}(-\mathbf{k})$ due to the DMI. The Hamiltonian is diagonalized by generalized Bogoliubov transformation (see Supplemental material: stacks.iop.org/JPhysCM/28/47LT02/mmedia). The positive eigenvalues are given by

$$\epsilon_{\alpha,\pm}(\mathbf{k}) = (-1)^{\alpha}h + \sqrt{\left[\epsilon_0\pm\sqrt{m^2_{\mathbf{k}\phi}+|v_s f_{\mathbf{k}}|^2}\right]^2 - v^2_{\perp}}. \quad (10)$$

For $h=0$, the energy bands are doubly degenerate — one of the major differences between ferromagnetically and antiferromagnetically coupled layers. Also notice that antiferromagnetically coupled layers have a linear dispersion near $\boldsymbol{\Gamma}$ (see Fig. 2(b)) as opposed to a quadratic dispersion in the ferromagnetic case. For $v_{\perp}=0$, Eq. 10 decouples and reduces to Eq. 6 with opposite magnetic field on each layer.

C. Bilayer antiferromagnetic insulator

In the fully antiferromagnetic case, each layer is modeled by the Heisenberg antiferromagnet, with $J, J', J_{\perp}<0$. Due the J' term, the Heisenberg antiferromagnet is frustrated as opposed to the ferromagnetic counterpart. With zero DMI $H^{\tau}_{DM}=0$, the system is considered to describe bilayer honeycomb antiferromagnetic material $Bi_3Mn_4O_{12}(NO_3)$ [34–38]. The ground state phase diagram of this model has been studied extensively [34–38].

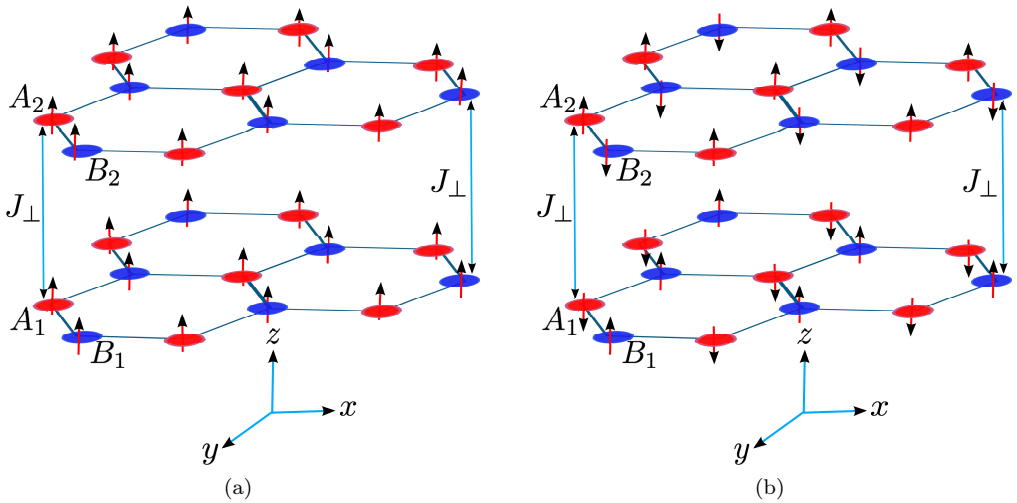

FIG. 1: Color online. (a) Ferromagnetically coupled AA-stacked bilayer honeycomb magnets. For antiferromagnetically coupled system, the spins on the upper or layer are pointing downwards. (b) AA-stacked honeycomb-lattice bilayer Néel antiferromagnet.

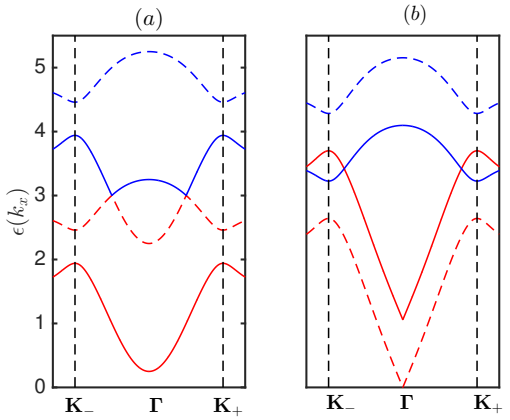

FIG. 2: Color online. Magnon band structures of spin-1/2 bilayer honeycomb chiral magnet for $h = v_s = 0.5$, $v_D = v_s' = 0.05$, $v_\perp = 1$, $\phi = \pi/4$. (a) Ferromagnetic coupling. (b) Antiferromagnetic coupling.

It consists of an ordered Néel state for $J'/J < 1/6$ and a nonmagnetic state for $J'/J > 1/6$ [34]. For large values of $J_\perp$, the ground state is an interlayer valence-bond crystal in which the spins from both layers form dimers [37].

We are interested in the topological effects of the ordered Néel state for $J'/J < 1/6$ shown in Fig. 1(b). Such Néel state order exists in the bilayer honeycomb iridates A_2IrO_3 (A= Na, Li) [29, 30]. In this phase, the band structure in the absence of the chiral DMI exhibits Dirac points at $\mathbf{K}_\pm = (\pm 4\pi/3\sqrt{3}a, 0)$ [35–38]. A nearest-neighbour DMI does not introduce chirality and an external magnetic field introduces canting up to the saturated field when fully polarized ferromagnetic states are recovered. These terms do not open a gap at $\mathbf{K}_\pm$. As in the ferromagnetic case, chirality is introduced by a next-nearest-neighbour DMI. As we now show, this is very similar to antiferromagnetically coupled bilayer ferromagnets studied above at zero magnetic field. The only difference is that the NNN coupling is restricted to $J'/J < 1/6$.

We begin by performing the π-rotation describe above on sublattice A_1 and B_2 such that the spins point along the new rotated z-axis. The SU(2)-invariant NN and NNN interactions on each layer are invariant under this rotation, but the U(1)-invariant out-of-plane DMI changes sign as in the previous case. In the bosonic representation, the Hamiltonian has the form as Eq. 8 with

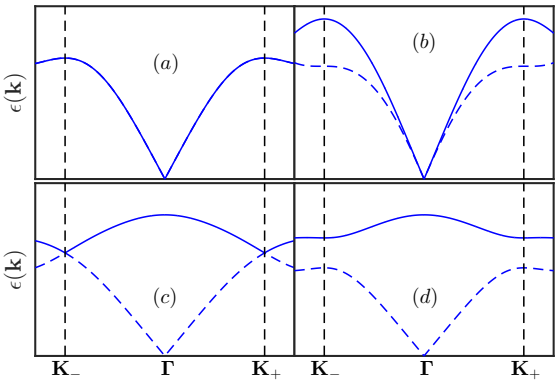

FIG. 3: Color online. Magnon bulk bands of the spin-1/2 AA-stacked bilayer Néel antiferromagnet along $k_y = 0$ at $h = 0$. The parameters are $v_s = 0.5$ (a). $v_D = v_\perp = 0$; $v_s' = 0.05$. (b). $v_\perp = v_s' = 0.0$, $v_D = 0.05$, $\phi = \pi/2$. (c). $v_\perp = v_s' = 0.05$, $v_D = 0.0$, $\phi = 0$; (d). $v_D = v_s' = 0.05$, $v_\perp = 0.5$, $\phi = \pi/4$.

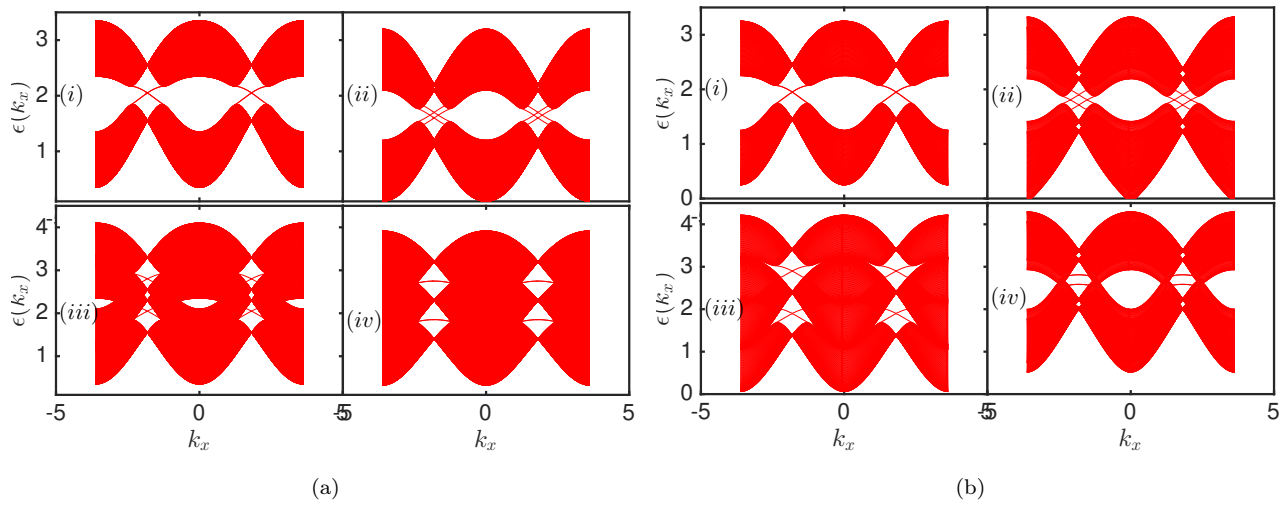

FIG. 4: Color online. Chiral edge states of AA-stacked bilayer honeycomb chiral magnets with $v_s = 0.5$. (a) Ferromagnetically coupled layers (i) $v_D = 0.1,\ v_s' = 0.05,\ h = 0.1,\ v_\perp = 0$. (ii) $v_D = 0.1,\ v_s' = 0.0,\ h = 0.1,\ v_\perp = 0.05$. (iii) $v_D = 0.1,\ v_s' = 0.05,\ h = 0.1,\ v_\perp = 0.375$. (iv) $v_D = 0.0,\ v_s' = 0.05,\ h = 0.1,\ v_\perp = 0.5$. (b) Antiferromagnetically coupled layers (i) $v_D = 0.1,\ v_s' = 0.05,\ h = v_\perp = 0$. (ii) $v_D = 0.1,\ v_s' = 0.0,\ h = 0.1,\ v_\perp = 0.5$. (iii) $v_D = 0.1,\ v_s' = 0.05,\ h = 0.5,\ v_\perp = 0.5$. (iv) $v_D = 0.0,\ v_s' = 0.05,\ h = 0.1,\ v_\perp = 0.5$.

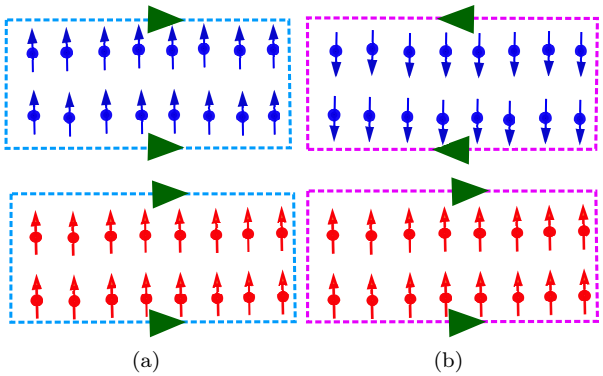

FIG. 5: Color online. Schematics of chiral edge states (green arrows). (a) Ferromagnetically coupled layers. (b) Antiferromagnetically coupled layers.

$$\mathcal{A}(\mathbf{k}) = \epsilon_0\tau_0 \otimes \sigma_0 + m_{\mathbf{k}\phi}\tau_z \otimes \sigma_0, \tag{11}$$
$$\mathcal{B}(\mathbf{k}) = v_s\tau_0 \otimes (f_{\mathbf{k}}\sigma_+ + f_{\mathbf{k}}^*\sigma_-) + |v_\perp|\tau_x \otimes \sigma_0, \tag{12}$$

where $\epsilon_0 = zv_s - z'|v_s'| + |v_\perp| + 2v_t\sum_\mu \cos(\mathbf{k}\cdot\mathbf{a}_\mu)\cos\phi$. As before $\mathcal{A}(\mathbf{k}) \neq \mathcal{A}^*(-\mathbf{k})$, but $\mathcal{B}(\mathbf{k}) = \mathcal{B}^*(-\mathbf{k})$. The Hamiltonian is diagonalized as usual. The positive eigenvalues are given by

$$\epsilon_{\alpha\pm}(\mathbf{k}) = \sqrt{m_{\mathbf{k}\phi}^2 + \epsilon_0^2 - v_\perp^2 - |v_s f_{\mathbf{k}}|^2 \pm 2g_{\mathbf{k}}}, \tag{13}$$

where $g_{\mathbf{k}} = \sqrt{m_{\mathbf{k}\phi}^2(\epsilon_0^2 - |v_s f_{\mathbf{k}}|^2) + |v_\perp v_s f_{\mathbf{k}}|^2}$. The band structures depicted in Fig. 3 are very similar to that of bilayer ferromagnet with antiferromagnetic coupling for $h = 0$. As mentioned above, a finite magnetic field introduces spin canting. In this case, both the out-of-plane and in-plane DMIs contribute to the magnon excitations. This scenario is analyzed in the Supplemental material: stacks.iop.org/JPhysCM/28/47LT02/mmedia.

IV. MAGNON TRANSPORTS

A. Magnon edges states

Magnetic transports in topological magnon insulator materials are encoded in the protected chiral edge states of the system induced by the DMI. Figure 4(a) shows the evolution of the chiral protected edge states of the ferromagnetically coupled layers in different parameter regimes. The chiral edge states propagate in the same direction as depicted schematically in Fig. 5(a). For antiferromagnetically coupled case, the same situation is observed with different parameters as depicted in Fig. 4(b). However, the chiral edge states propagate in opposite directions for the top and bottom layers because of opposite DMI as shown schematically in Fig. 5(b).

B. Magnon Hall effect

The most interesting property of chiral magnetic systems is the observation of magnon Hall effect [2, 4, 18, 19]. In magnon Hall effect [1], as well as magnon spin Nernst effect [24], the non-vanishing Berry curvatures induce an effective magnetic field in the system, upon the ap-

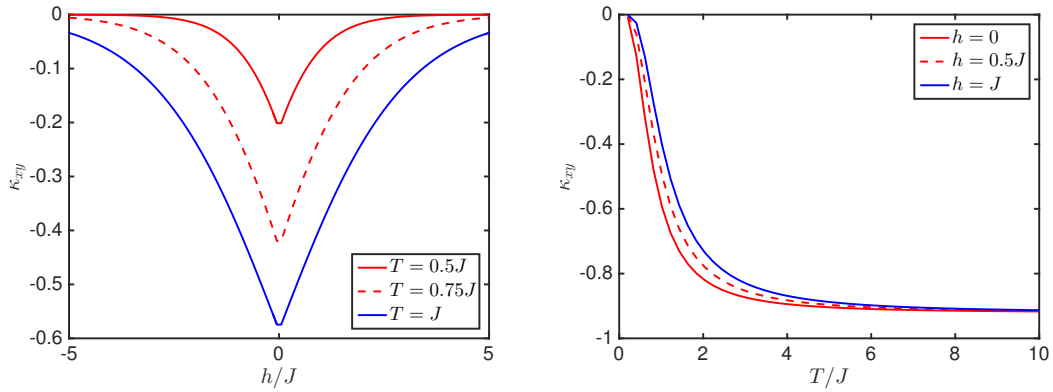

FIG. 6: Color online. Thermal Hall conductivity of ferromagnetically coupled AA-stacked bilayer honeycomb chiral magnet as function of (a) magnetic field (b) temperature. The parameters are the same as Fig. 2 (a).

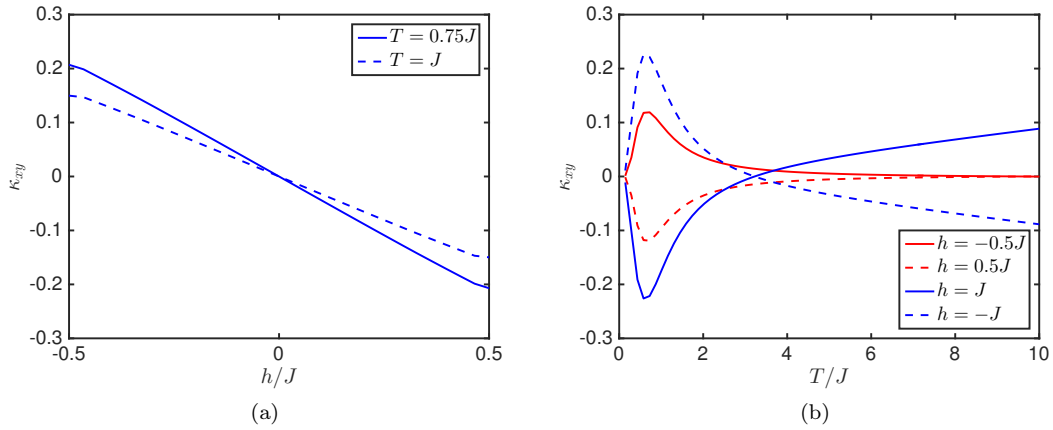

FIG. 7: Color online. Thermal Hall conductivity of antiferromagnetically coupled AA-stacked bilayer honeycomb chiral magnet as function of (a) magnetic field (b) temperature. The parameters are the same as Fig. 2 (b).

plication of a temperature gradient. The propagation of magnons in the bilayer system is deflected by the chiral DMI. Magnon Hall effect is characterized by a transverse thermal Hall conductivity, given by [3] $\kappa_{xy} = -2k_B^2 T V^{-1} \sum_{\mathbf{k}\mu} c_2\left(n_\mu\right) \Omega_\mu(\mathbf{k})$, where V is the volume of the system, k_B is the Boltzmann constant, T is the temperature, $n_\mu \equiv n_B[\epsilon_\mu(\mathbf{k})] = [e^{\epsilon_\mu(\mathbf{k})/k_B T} - 1]^{-1}$ is the Bose function, $c_2(x) = (1+x)\left(\ln\frac{1+x}{x}\right)^2 - (\ln x)^2 - 2\mathrm{Li}_2(-x)$, and $\mathrm{Li}_2(x)$ is a dilogarithm. Magnon spin Nernst conductivity has a similar definition [24] $\alpha^s_{xy} = k_B V^{-1} \sum_{\mathbf{k}\mu} c_1\left(n_\mu\right) \Omega_\mu(\mathbf{k})$, where $c_1(x) = (1+x)\ln(1+x) - x\ln x$. The chirality-induced Berry curvature is defined as

$$\Omega_\mu(\mathbf{k}) = -2 \sum_{\mu \neq \mu'} \frac{\mathrm{Im}[\langle\psi_{\mathbf{k}\mu}|v_x|\psi_{\mathbf{k}\mu'}\rangle \langle\psi_{\mathbf{k}\mu'}|v_y|\psi_{\mathbf{k}\mu}\rangle]}{[\epsilon_{\mathbf{k}\mu} - \epsilon_{\mathbf{k}\mu'}]^2}, \quad (14)$$

where $|\psi_{\mathbf{k}\mu}\rangle$ are the eigenstates of the Hamiltonian and μ labels the bands; $v_{x,y} = \partial\mathcal{H}(\mathbf{k})/\partial k_{x,y}$ defines the velocity operators.

Figures 6(a) and 6(b) show the dependence of thermal Hall conductivity on the magnetic field and the temperature for the ferromagnetically coupled layers. As the temperature approaches zero, κ_{xy} vanishes due to lack of thermal excitations, but it never changes sign as the temperature increases or the magnetic field changes sign. This is what is observed theoretically in the single layer honeycomb chiral ferromagnet [22]. However, for antiferromagnetically coupled layers shown in Figs. 7(a) and 7(b), we see that κ_{xy} changes sign as the magnetic field is reversed and vanishes at zero field. The sign change in κ_{xy} is encoded in the magnon bulk bands, the Berry curvatures, and the propagation of the chiral edge states. The sign change in κ_{xy} is very similar to what was observed on the pyrochlore chiral magnets upon reversing the direction of the applied magnetic field [2, 3]. Due to the Berry curvature, α^s_{xy} shows similar trends (not shown). We also observe that for the chirality-proximity effect, where only one

layer contains a chiral DMI, topological effects are induced in the bilayer system and thermal conductivity κ_{xy} is suppressed (see the Supplemental material: stacks.iop.org/JPhysCM/28/47LT02/mmedia).

V. CONCLUSION

We have studied chirality-induced magnon transport in AA-stacked bilayer honeycomb chiral magnets. We observe remarkable distinctive features for ferromagnetic and antiferromagnetic couplings. In particular, the band structure and the chiral edge states have different topological properties. As a result thermal Hall and spin Nernst conductivities show a sign change for antiferromagnetic coupling in contrast to ferromagnetic coupling. As far as we know, chirality-induced transports and thermal Hall effect still await experimental observation on the honeycomb lattice. As mentioned above, there are many accessible AA-stacked bilayer honeycomb quantum magnets in which chirality can be induced and these theoretical results can be confirmed. Experiments can also probe the observed magnon edge states, by noticing that spin-1/2 quantum magnets map to hardcore bosons. Thus, the magnon edge states correspond to bosonic edge states, which can be studied experimentally in ultracold atoms on optical lattices similar to the realization of Haldane model [39]. Our results can also be applied to magnon spintronics in chiral bilayer quantum magnetic systems.

Acknowledgments

Research at Perimeter Institute is supported by the Government of Canada through Industry Canada and by the Province of Ontario through the Ministry of Research and Innovation.

[1] H. Katsura, N. Nagaosa, and P. A. Lee, Phys. Rev. Lett. **104**, 066403 (2010).
[2] S. Y. Onose *et al.*, Science **329**, 297 (2010).
[3] R. Matsumoto and S. Murakami, Phys. Rev. Lett. **106**, 197202 (2011); Phys. Rev. B **84**, 184406 (2011).
[4] T. Ideue *et al.*, Phys. Rev. Lett. **85**, 134411 (2012).
[5] L. Zhang, J. Ren, J. S. Wang, and B. Li, Phys. Rev. B **87**, 144101 (2013).
[6] A. Mook, J. Henk, and I. Mertig, Phys. Rev. B **90**, 024412 (2014); *ibid*, Phys. Rev. B **89**, 134409 (2014).
[7] H. Lee, J. H. Han, and P. A. Lee, Phys. Rev. B. **91**, 125413 (2015).
[8] Xichao Zhang, Yan Zhou , and Motohiko Ezawa, Nature Communications **7**, 10293 (2015).
[9] R. Shindou et.al., Phys. Rev. B 87, 174427 (2013); Phys. Rev. B 87, 174402 (2013).
[10] R. Matsumoto, R. Shindou, and S. Murakami, Phys. Rev. B 89, 054420 (2014).
[11] M. Z. Hasan and C. L. Kane, Rev. Mod. Phys. **82**, 3045 (2010).
[12] X. -L. Qi and S. -C. Zhang, Rev. Mod. Phys. **83**, 1057 (2011).
[13] F. D. M. Haldane, Phys. Rev. Lett. **61**, 2015 (1988).
[14] V. V. Kruglyak, S. O. Demokritov, and D. Grundler, J. Phys. D: Appl. Phys. **43**, 264001 (2010).
[15] B. Lenk, H. Ulrichs, F. Garbs, M. Münzenberg, Physics Reports **507**, 107 (2011).
[16] A. V. Chumak, V. I. Vasyuchka, A. A. Serga and B. Hillebrands, Nature Physics **11**, 453 (2015).
[17] I. Dzyaloshinsky, J. Phys. Chem. Solids **4**, 241 (1958); T. Moriya, Phys. Rev. **120**, 91 (1960).
[18] R. Chisnell *et al.*, Phys. Rev. Lett. **115**, 147201 (2015).
[19] M. Hirschberger *et al.*, Phys. Rev. Lett. **115**, 106603 (2015).
[20] X. Cao, K. Chen and D. He, J. Phys.: Condens. Matter **27**, 166003 (2015).
[21] S. A. Owerre, J. Phys.: Condens. Matter **28**, 386001 (2016).
[22] S. A. Owerre, J. Appl. Phys. **120**, 043903 (2016).
[23] S. K. Kim *et al.*, arXiv:1603.04827.
[24] A. A. Kovalev and V. Zyuzin, Phys. Rev. B **93**, 161106(R) (2016).
[25] A. C. Gossard, V. Jaccarino, and J. P. Remeika, Phys. Rev. Lett. **7**, 122 (1961)
[26] H. L. Davis and Albert Narath, Phys. Rev. **134**, A433 (1964).
[27] Y. Miura *et al.*, J. Phys. Soc. Jpn. **75**, 084707 (2006).
[28] A. A. Tsirlin, O. Janson, and H. Rosner, Phys. Rev. B **82**, 144416 (2010);
[29] Y. Singh *et al.*, Phys. Rev. B **82**, 064412 (2010); Phys. Rev. Lett. **108** 127203 (2012); S. Okubo *et al.*, J. Phys.: Conf. Ser. **200**, 022042 (2010).
[30] X. Liu *et al.*, Phys. Rev. B **83**, 220403(R) (2011); S. K. Cho *et al.*, Phys. Rev. Lett. **108**, 127204 (2012).
[31] T. Holstein and H. Primakoff, Phys. Rev. **58**, 1098 (1940).
[32] E. Prada, P. San-Jose, L. Brey, and H. A. Fertig, Solid State Commun. 151, 1075 (2011).
[33] C. J. Tabert and E. J. Nicol, Phys. Rev. B 86, 075439 (2012).
[34] A. Mulder, R. Ganesh, L. Capriotti, and A. Paramekanti, Phys. Rev. B. **81**, 214419 (2010).
[35] R. Ganesh, D. N. Sheng, Young-June Kim, and A. Paramekanti1, Phys. Rev. B. **83**, 144414 (2011).
[36] J. Oitmaa and R. R. P. Singh, Phys. Rev. B. **85**, 014428 (2012).
[37] Hao Zhang, M. Arlego, and C. A. Lamas, Phys. Rev. B. **89**, 024403 (2014).
[38] F. A. Gómez Albarracín and H. D. Rosales, Phys. Rev. B. **92**, 144413 (2016).
[39] G. Jotzu *et al*, Nature **515**, 237 (2014).